Powerful Acoustogeometric Streaming from Dynamic Geometric Nonlinearity

Naiqing Zhang, Amihai Horesh, Ofer Manor, and James Friend

Powerful acousto-geometric streaming from dynamic geometric nonlinearity

Naiqing Zhang,[1] Amihai Horesh,[1] Ofer Manor,[2] James Friend[1]

[1] *Medically Advanced Devices Laboratory, Department of Mechanical and Aerospace Engineering,*
Jacobs School of Engineering, and Department of Surgery,
School of Medicine, University of California San Diego,
9500 Gilman Dr. MC0411 La Jolla, CA 92093 USA
[2] *Wolfson Department of Chemical Engineering, Technion—Israel Institute of Technology, Haifa 3200003 Israel*

Past forms of acoustic streaming, named after their progenitors Eckart (1948), Schlichting (1932), and Rayleigh (1884), serve to describe fluid and particle transport phenomena from macro to micro scales. Governed by the fluid viscosity, traditional acoustic streaming arises from second-order nonlinear coupling between the fluid's density and particle velocity, with the first-order acoustic wave time-averaging to zero. We describe a form of acousto-geometric streaming that has a non-zero first-order contribution. Experimentally discovered in nanochannels of a height commensurate with the viscous penetration depth of the fluid in the channel, it arises from nonlinear interactions between the surrounding channel deformation and the leading order acoustic pressure field, generating flow pressures three orders of magnitude greater than any known acoustically-mediated mechanism. It enables the propulsion of fluids against significant Laplace pressure, sufficient to produce 6 mm/s flow in a 130–150 nm tall nanoslit. We find quantitative agreement between theory and experiment across a variety of fluids and conditions, and identify the maximum flow rate with a channel height 1.59 times the viscous penetration depth.

The potential of novel biological analysis and sensing, medical diagnosis, and material processing makes nanofluidics [1] an enticing research area, if not for the challenges of fluid transport at this scale. Because surface-mediated forces are overwhelmingly dominant, wetting and dewetting and the manipulation of fluid interfaces all play a key role in nanoscale fluid transport.

Acoustic waves and the acoustic streaming they generate [2] have long been proposed in various forms—including, in particular, surface acoustic waves (SAW) [3–5]—to produce fluid and particle transport at the milli to micro-scale. Among the many examples, Schneider *et al.* reported flow in a microfluidic racetrack structure with low resistance [6]. Both Cecchini *et al.* [7] and Girardo *et al.* [8] presented acoustic devices that used atomization to produce fluid transport in microchannels. Bauerle *et al.*, used SAW as a peristaltic pump to show that cost-efficiency of mass transport in peristalsis depends upon its phase modulation [9]. A recent paper [10] employed computation and theory to predict the motion of a fluid meniscus in a ~10 μm thick channel by using a propagating wave along the channel substrate. But the underpinning assumptions limit its validity, especially in our case: the particle velocity of the excitation is assumed to be small compared to the sound's phase velocity, eliminating compressibility and acoustic effects that are important in the mechanism we observe here.

Eckart streaming [11], driving bulk flow from viscous attenuation of acoustic waves, is responsible for many of the results described in the macro-to-micro-scale applications of the previous paragraph [2–6]. Other forms of acoustic streaming identified by Rayleigh [12] and Schlichting [13] prior to Eckart streaming also may be found in some of these results, and appear, respectively,
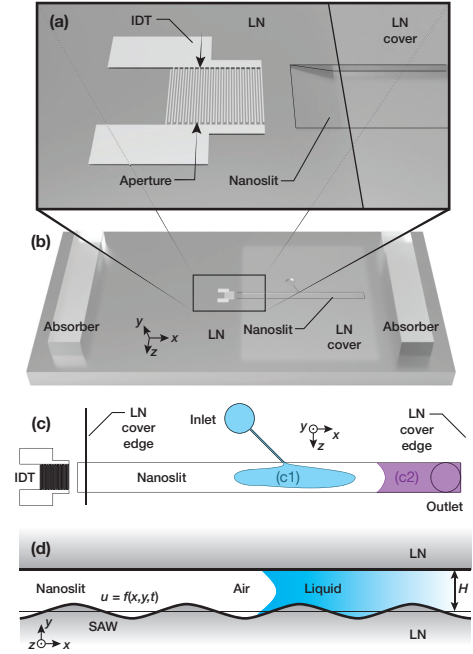

FIG. 1. An (a) IDT with a 625 μm wide aperture produces SAW that propagates (b) underneath an aligned, 1-mm wide, 5-mm long nanoslit etched into the LN substrate with a room-temperature bonded LN cover. Absorbers eliminate reflected waves. The channel depth is *greatly* exaggerated for clarity. (c) A 20-μm wide, 500-μm long side channel, which controls the filling rate, connects the main channel at 45° to the 1-mm diameter inlet well. A 1-mm diameter (c1) outlet present at the end of the nanoslit distal from the IDT provides a means for (c2) fluid outflow.

in the bulk and boundary layer of the fluid, driven by motion of the boundary. Other forms of acoustic streaming,

such as microstreaming [14, 15] and sharp-edge streaming [16, 17] are variations on these forms of acoustic streaming [3]. All are due to generation and convection of momentum flux, in turn dependent upon the spatiotemporal inertia from the Navier-Stokes equation and averaged over one or more time periods of the acoustic vibration [18]. The momentum flux is further associated with the spatial derivative of the time-averaged Reynolds stress in the liquid, $\langle \rho uu \rangle$, where ρ, u, and $\langle \cdot \rangle$ are the density and velocity in the liquid and a time-averaging operator, respectively [19, 20]. In acoustofluidics, typically $\rho \approx 1000$ kg/m^3 and $|u| \equiv U \sim 0.01 - 1$ m/s, where U is the amplitude of particle velocity of the acoustic wave.

Consequently, the characteristic magnitude of the Reynolds stress, and therefore the pressure these three forms of acoustic streaming may bring to bear on a fluid interface, is $\rho U^2 \approx 0.1 - 1000$ Pa, sufficient to overcome Laplace pressure of the liquid meniscus and enable dynamic wetting and de-wetting of micro to macro-scale channels. However, in submicron and smaller channels, acoustically-driven wetting and dewetting is overwhelmed by the meniscus' Laplace pressure, $\Delta P \approx \gamma \cos \theta / (H/2)$, where γ, θ, and H are the fluid-air interfacial surface tension; the three-phase contact angle between the fluid, air, and the lithium niobate substrate; and the thickness of the channel; respectively. The Laplace pressure is 0.1 MPa for a 1 μm thick channel, and grows with a decrease in the channel height. Furthermore, fluid viscosity and the dynamic resistance it presents to the flow must be overcome [21]. A Laplace pressure of $\Delta P \approx 14$ MPa to 1.4 MPa in a channel of thickness $H = 10$ nm to 100 nm, respectively, is far larger than the second-order acoustic streaming-mediated pressure [22] of the order $\rho U^2 \sim 0.1$–1000 Pa, assuming in this example that $\gamma \approx 70$ mN/m for deionized water and $\theta \approx 0°$ for the hydrophilic LN substrate. The acoustic *radiation* pressure [19] is *also* on the order of ρU^2, because the nanoslit channel's thickness is small compared to the wavelength of sound in the fluid, and is also insignificant.

By contrast, for the same 1 m/s particle velocity of the acoustic wave, the corresponding peak pressure is much larger. It is approximately $\rho U c_l \sim 1.5$ MPa. Here c_l is the phase velocity of sound in the liquid—water in this example. This pressure is equivalent to the Laplace pressure in a water-air meniscus within a 100-nm high hydrophilic channel, but it is harmonic, with a time average of zero. It is reasonable to assume that this leading order acoustic pressure is responsible for the observed transport [23] of liquid menisci in the nanochannels. However, for this to be true, there must be a rectifying mechanism that produces a net transport of the meniscus by the purely harmonic oscillation of the acoustic pressure. This mechanism was not explained in prior work [23], and is instead the focus of this paper, defined as acousto-geometric streaming from a dynamic geometric nonlinearity.

TABLE I. Physical parameters of the fluids and nanoslit channels used in our experiments.

	γ (mN/m)	μ (cP)	c_l (m/s)	ρ (kg/m^3)	δ (nm)	ω (10^8 rad/s)	H (nm)	H/δ (—)
Water	72	0.89	1482	997	86	2.42	150	1.75
IPA	22	1.96	1170	786	145	2.38	130	0.90
Methanol	22	0.543	1116	792	76	2.37	130	1.71
1-Octanol	27	7.36	1349	830	274	2.37	130	0.48

We now define an acoustic streaming mechanism that becomes significant as $H \sim \delta$, where $\delta = \sqrt{2\mu/\rho\omega}$ [24] is the viscous penetration depth for acoustic energy leakage into the fluid from SAW propagating along an adjacent boundary. Here μ and ω are the liquid's viscosity and the angular frequency of the SAW, respectively. Noting Fig. 1, δ is the length scale where the viscosity may affect the flow at the time scale of the acoustics, $1/\omega$. In our experiments, generally $\delta \sim 100$ nm and the ratio of the channel height to the boundary layer thickness is ~ 1; specific values are provided in Table I for the fluids in this study: water, IPA, methanol, and 1-octanol. Note the nanoslit is closer to the SAW device than the edge of the LN cover layer (*see* Fig. 1), leaving a gap that prevents SAW coupling into the top LN layer. This, and the fact the SAW aperture being less than the channel width leaves the SAW to propagate solely along the bottom boundary. To highlight this, we show a side view of the nanoslit in Fig. 1(d). This is a crucial difference from past work [23], where the SAW propagation along both the top and bottom boundaries was poorly controlled.

Neglecting the attenuation of the SAW due to acoustic energy leakage into the adjacent fluid, justified by noting the very small volume of fluid present in the nanoslit system, we assume that the deformation of the bottom channel surface by the SAW is given by

$$A = -|U/\omega| \cos (\omega [t - x/c_s]), \qquad (1)$$

with respect to its position at rest. Referring to Fig. 1, we also assume the width (along z) and length of the channel (along x) are large compared to its nominal height H (along y), and that the deformation is identical across the width of the channel. The deformation A is assumed to be purely in the y direction, while the wave carrying the deformation propagates along the x axis at the SAW's phase velocity c_s, where t is the time and $|A| = U/\omega$ is the amplitude of the channel wall's normal deformation.

The corresponding leading order acoustic pressure in the thin liquid film is

$$p = \rho c_l \partial A/\partial t = \rho U c_l \sin [\omega (t - x/c_s)]. \qquad (2)$$

We presume that x scales like the inverse of the wavelength of the SAW, $\kappa^{-1} \equiv c_s/\omega$ and that y scales like δ. The scaling for the pressure field $p \sim \rho U c_l$ is a product of eqn. (2). The tangent (in the x direction) and normal (in the y direction) flow velocities along the channel, u

and v, respectively, satisfy to leading order a solenoidal vector field and are governed by the continuity equation $\partial u/\partial x + \partial v/\partial y = 0$. Hence, the velocity field may be scaled according to $u \sim \kappa\delta U$ and $v \sim U$. While in practice the acoustic effect responsible for the pressure undulation in (2) is due to small variations in the density, these variations do not contribute at the order of magnitude of the flow field in our discussion.

The corresponding leading-order terms in the Navier-Stokes equations, assuming that $\kappa\delta \ll 1$, $U/c_l \ll 1$, and $\mu\kappa/\rho c_l \ll 1$ to match our experiments, produce

$$\rho\frac{\partial u}{\partial t} - \mu\frac{\partial^2 u}{\partial y^2} + \frac{\partial p}{\partial x} = 0; \qquad \frac{\partial p}{\partial y} = 0, \qquad (3)$$

subject to eqn. (2) and a vanishing flow velocity at the channel walls. A Galilean transformation, $u = \Re\left\{-\iota f(y)e^{\iota\omega(t-x/c_s)}\right\}$ and $p = \Re\left\{-\iota\rho U c_l e^{\iota\omega(t-x/c_s)}\right\}$, simplifies the analysis, where $\Re(\cdot)$ is the real part and $\iota \equiv \sqrt{-1}$. This simplifies to the boundary value problem

$$f''(y) - \frac{\iota\rho\omega}{\mu}f(y) + \frac{\iota c_l\rho U\omega}{c_s\mu} = 0, \qquad (4)$$

subject to $f = 0$ at $y = \{0,h\}$, where $h \equiv H - A(x,t)$ is the local spatiotemporal thickness of the excited channel and $A(x,t)$ is given in eqn. (1). With these boundary conditions, eqn. (4) is satisfied by $f(y) = C_1 \exp\left[(1+\iota)\frac{y}{\delta}\right] + C_2 \exp\left[-(1+\iota)\frac{y}{\delta}\right] - \iota c_l U/c_s$, where $C_1 = \iota c_l c_s U \left\{1 + \exp\left[(1+\iota)\frac{h}{\delta}\right]\right\}^{-1}$ and $C_2 = C_1 \exp\left[(1+\iota)\frac{h}{\delta}\right]$.

Substituting $h = H - A(x,t)$ for u in the Galilean transformation above and averaging over a long time—equivalent here to averaging over one time period of the acoustic wave—produces the leading order time-averaged volume flux per unit width of the channel, $\langle Q\rangle = \frac{1}{T}\int_0^T Q\,dt$. Expanding the solution in the small parameter $|A|/\delta \ll 1$, integrating over the local channel spatiotemporal thickness, h, and dividing the result by the channel thickness at rest, H, gives us the average flow velocity in the channel,

$$\frac{\langle u\rangle}{Uc_l/c_s} = \frac{\langle Q\rangle}{UHc_l/c_s} = \frac{|A|}{H}\frac{\sin\left(\frac{H}{\delta}\right)\sinh\left(\frac{H}{\delta}\right)}{\left(\cos\left(\frac{H}{\delta}\right) + \cosh\left(\frac{H}{\delta}\right)\right)^2}. \quad (5)$$

Hence, the meniscus velocity $\langle u\rangle$ is scaled by the ratio of the deformation amplitude to the thickness of the channel, $|A|/H$. The Supplemental Information (SI) includes a simplification of this equation for $H/\delta \ll 1$ at [publisher URL]. This motion is reminiscent of a peristaltic pump, with the key difference that the flow is generated here via acoustic pressure and traditional peristaltic pumps rely on hydrodynamic pressure.

As $H/\delta \to 0$, the volume flux $\langle Q\rangle \to 0$ vanishes as expected. However, as H/δ and the channel height are increased, the volume flux $\langle Q\rangle$ increases to a maximum of $\langle Q\rangle = 0.366 c_l U^2/(c_s\omega)$ at $H/\delta = 1.59$ before decreasing

to zero at $H/\delta \gtrsim 3$. There is no first-order acoustically-induced flow if the channel height is even modestly large compared to the viscous penetration depth. This does not necessarily imply the absence of acoustically driven flow, however, as second and higher-order non-linear effects—traditional forms of acoustic streaming—may cause relatively weak fluid transport.

We now turn to experimental evidence of the phenomena, employing SAW at 38.5 MHz along nanoslits fabricated to have heights on the order of the viscous penetration depth, $H \approx \delta/2 - 2\delta$. The nanoslit fabrication process is detailed in past work [23, 25], but details specific to this letter are provided in the SI at [publisher URL] as is information on the SAW generation and measurement methods. Briefly, a laser Doppler vibrometer (LDV, UHF–120, Polytec, Waldbronn, Germany) was used to measure the y-axis oriented, out-of-plane particle velocity of the SAW upon the LN substrate surface, making it possible to determine the acoustic power transmitted by the SAW from the IDT. Notably, the longitudinal component of the SAW along the x axis is not measured, but is both known to be about 0.8 of the y-axis oriented motion in LN and weakly coupled to a fluid if present on the surface [3].

Liquid introduced into the fluid reservoir first fills the side channel, from which the main channel slowly fills, displacing the air present in the system. Once the meniscus reached equilibrium, we activated the SAW propagating from the IDT and along the nanoslit channel, as shown in Fig. 1. Note that the axial filling asymmetry in these images is due to the application of SAW.

Applying SAW causes the trailing edge liquid meniscus—closer to the IDT—to be propelled away from the IDT and towards the outlet reservoir. The velocity of the meniscus, shown in Fig. 2, appears proportional to the acoustic power. This was the case with water, isopropyl alcohol (IPA), methanol, and 1-octanol, fluids of significantly different properties (*see* Table I). The meniscus velocities across these fluid choices and for multiple runs collapse onto a single curve in Fig. 2 upon application of the scaling defined in eqn. (5). Moreover, the experiment is in quantitative agreement with theory, notable as the latter is a consequence of the nonlinear coupling between the first-order acoustic field in the fluid and the harmonic change of the channel height with the passage of the SAW.

The time-averaged volume flux per channel width $\langle Q\rangle$ mainly depends upon the ratio of slit height to viscous boundary layer thickness H/δ when using a fixed power and frequency, as represented by $(|A|UH)/H \sim U^2/\omega$ in eqn. (5). This occurs because the sound velocity c_l is the same order of magnitude for most fluids, including those we considered.

Capillary forces are comparatively insignificant. The average capillary filling velocity may be derived using a straightforward rearrangement of the classic Washburn
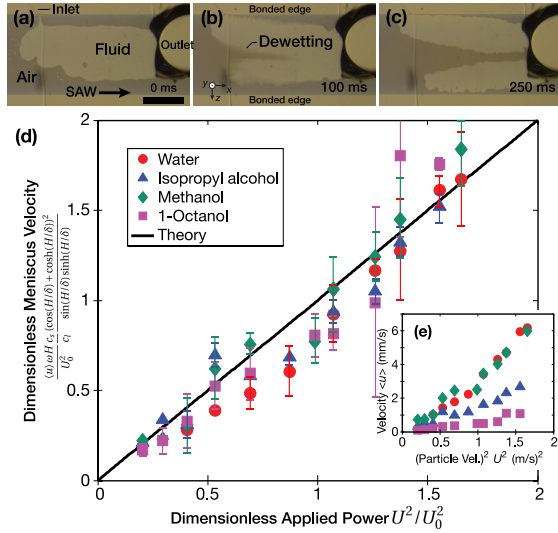
FIG. 2. (a,b,c) Fluid transport and meniscus dewetting deionized water from within a 150 nm-thick hydrophilic nanoslit using ~ 1 W, 38.5 MHz SAW, and applied from 0 ms. Scale bar: 0.5 mm. With different fluids, the meniscus velocity versus the applied power, (d) nondimensionalized using eqn. (5), where $U_0 = 1$ m/s is the scaled velocity, collapses the onto a line from the (e) original dimensional results. The theory is effective in representing the observed phenomena. Drainage of other fluids and videos and a version of (e) dimensional fluid velocity versus applied power with error bars are all in the SI at [publisher URL]. Error bars indicate the max-min range of the data for each point ($N \geq 10$).
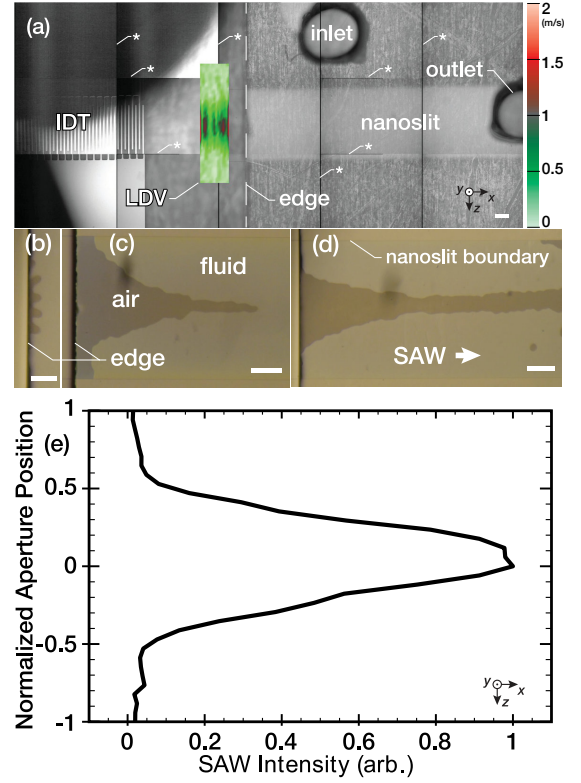

FIG. 3. (a) The $H = 150$ nm nanoslit and IDT generating 38.5-MHz SAW from left to right with 1 W input power. An LDV-measured SAW velocity amplitude contour plot is shown before it propagates underneath the nanoslit. The color bar showing normalized SAW particle velocity amplitude from 0 to 1 is presented on the right of the image. Due to the scale, image stitching was necessary with *boundaries indicated. The initial (b) dewetting of the fluid—water in this case, *see* Table I for dimensions and details—from the edge of the nanoslit by SAW illustrates the effect of near-field Fresnel diffraction. This evolves to a (c) steady-state meniscus deformation into the nanoslit at 394 mW, the depth of which depends on the SAW amplitude. Increasing the SAW power, to 830 mW, (d) drains the water along the entire length of the nanoslit. In (e) the intensity of the SAW ($\propto U^2$) is plotted across the width of the IDT aperture, indicating why there is a (c,d) narrow channel of flow: the flow is most significant where the SAW intensity is large. Scale bar: 0.2 mm.

model [23, 26] as shown in the SI at [publisher URL]. We may then calculate this velocity from experimental data *without SAW* to be $\bar{v} = \gamma H \cos\theta/(3\mu) \sim 0.4$ mm/s, a time-averaged volume flux per unit width for a 150-nm high channel of 60 μm^2/s. This is one order of magnitude less than the new acoustic streaming mechanism.

We now turn to the first known observations of liquid meniscus instabilities in a nanoscale fluid channel, as illustrated in Fig. 3. Since the IDT responsible for generating the SAW has a finite aperture, near-field and far-field diffraction [27] generates an evolving, non-uniform amplitude distribution across the width of the propagating SAW. This produces corresponding variations in the speed at which the fluid meniscus advances within the nanochannel. Resembling viscous and granular fingering instabilities [28–30] and thin-film instabilities [31], the mechanism and phenomena here are unique, especially the rapid dewetting against MPa-order capillary pressures in a nanoslit.

In the near-field of the SAW (Fig. 3(a)) emanating from the IDT to the right [32], the water meniscus initially exhibits fingering corresponding to near-field SAW diffraction as it begins to de-wet the nanoslit in Fig. 3(b). In the far-field of the SAW at 394 mW, the near-Gaussian amplitude distribution drives a corresponding dewetting profile at equilibrium in Fig. 3(c). Increasing the in-put power to 830 mW causes the meniscus to be completely dewetted along a narrow region at the center of the nanoslit in Fig. 3(d). Beyond the fact the majority of the SAW is passing at the center of the nanoslit, as determined from the intensity of the SAW measured in the far field of the SAW at over 20λ away from the IDT and shown in Fig. 3(e), there is slight lateral infill of the fluid to narrow this dewetting region. The lateral distribution of the SAW intensity significantly changes from the near field to the far field, but upon reaching the far field remains relatively constant. The close correspondence between the SAW intensity in Fig. 3(e) at 394 mW and the meniscus displacement in Fig. 3(c,d) is

interesting. However, the reader should remember that with greater power the meniscus can have a substantially different shape than the SAW intensity due to dewetting. The key point is that the meniscus displacement will be far lower at the edges because the SAW energy is concentrated near the center of the aperture and channel.

Because the nanoslit also has a finite width, the fluid laterally infills along the z axis to narrow the meniscus, but is prevented from completely refilling the channel due to the presence of a strong gradient in the acoustic energy, E, along the z axis from the edge of the nanoslit to the center as indicated in Fig. 3(d). The gradient produces an acoustic force from $F = \partial E / \partial z$ oriented towards the nanoslit sides and in opposition to the inward-facing capillary force. The net result is a slightly more narrow dewetting region than might be expected based upon the far-field SAW amplitude distribution alone.

---

[1] R. B. Schoch, J. Han, and P. Renaud, Reviews of Modern Physics **80**, 839 (2008).

[2] W. L. Nyborg, The Journal of the Acoustical Society of America **25**, 68 (1953).

[3] J. Friend and L. Y. Yeo, Reviews of Modern Physics **83**, 647 (2011).

[4] X. Ding, P. Li, S.-C. S. Lin, Z. S. Stratton, N. Nama, F. Guo, D. Slotcavage, X. Mao, J. Shi, F. Costanzo, *et al.*, Lab on a Chip **13**, 3626 (2013).

[5] W. Connacher, N. Zhang, A. Huang, J. Mei, S. Zhang, T. Gopesh, and J. Friend, Lab on a Chip **18**, 1952 (2018).

[6] S. Schneider, S. Nuschele, A. Wixforth, C. Gorzelanny, A. Alexander-Katz, R. Netz, and M. F. Schneider, Proceedings of the National Academy of Sciences **104**, 7899 (2007).

[7] M. Cecchini, S. Girardo, D. Pisignano, R. Cingolani, and F. Beltram, Applied Physics Letters **92**, 104103 (2008).

[8] S. Girardo, M. Cecchini, F. Beltram, R. Cingolani, and D. Pisignano, Lab on a Chip **8**, 1557 (2008).

[9] F. K. Bäuerle, S. Karpitschka, and K. Alim, Physical Review Letters **124**, 098102 (2020).

[10] E. de Jong, J. M. J. Den Toonder, and P. R. Onck, Physical Review Fluids **5**, 063604 (2020).

[11] C. Eckart, Physical Review **73**, 68 (1948).

[12] L. Rayleigh, Philosophical Transactions of the Royal Society of London **175**, 1 (1884).

[13] H. Schlichting, Phys. z. **33**, 327 (1932).

[14] A. A. Doinikov and A. Bouakaz, The Journal of the Acoustical Society of America **127**, 703 (2010).

[15] X. Liu and J. Wu, The Journal of the Acoustical Society of America **125**, 1319 (2009).

[16] M. Ovchinnikov, J. Zhou, and S. Yalamanchili, The Journal of the Acoustical Society of America **136**, 22 (2014).

[17] N. Nama, P.-H. Huang, T. J. Huang, and F. Costanzo, Lab on a Chip **14**, 2824 (2014).

[18] J. Lighthill, Journal of Sound and Vibration **61**, 391 (1978).

[19] B.-T. Chu and R. E. Apfel, The Journal of the Acoustical Society of America **72**, 1673 (1982).

[20] M. F. Hamilton and D. T. Blackstock, eds., *Nonlinear Acoustics* (Acoustical Society of America, 2008).

[21] T. M. Squires and S. R. Quake, Reviews of Modern Physics **77**, 977 (2005).

[22] A. A. Doinikov, P. Thibault, and P. Marmottant, Physical Review E **96**, 013101 (2017).

[23] M. Miansari and J. R. Friend, Advanced Functional Materials **26**, 7861 (2016).

[24] P. M. Morse and K. U. Ingard, *Theoretical Acoustics* (Princeton University Press, 1986).

[25] N. Zhang and J. Friend, JoVE (Journal of Visualized Experiments) , e60648 (2020).

[26] E. W. Washburn, Physical Review **17**, 273 (1921).

[27] T. L. Szabo and A. Slobodnik, IEEE transactions on Sonics and Ultrasonics **20**, 240 (1973).

[28] A. Cazabat, F. Heslot, S. Troian, and P. Carles, Nature **346**, 824 (1990).

[29] O. Pouliquen, J. Delour, and S. B. Savage, Nature **386**, 816 (1997).

[30] X. Cheng, L. Xu, A. Patterson, H. M. Jaeger, and S. R. Nagel, Nature Physics **4**, 234 (2008).

[31] A. Rezk, O. Manor, L. Y. Yeo, and J. R. Friend, Proceedings of the Royal Society A **470** (2014).

[32] The leftward-propagating SAW from the IDT is absorbed and suppressed.